

CONAN—Novel Tool to Create and Analyze Liquids in Confined Space

Leonard Dick and Barbara Kirchner*



Cite This: *J. Chem. Inf. Model.* 2023, 63, 6706–6716



Read Online

ACCESS |

Metrics & More

Article Recommendations

Supporting Information



ABSTRACT: Modeling of complex liquids at solid surfaces and in confinement is gaining attention due to an increase in computer power and advancement of simulation techniques. Therefore, tools to set up structures and for analysis are needed. In this paper, we present CONAN—a Python code designed to facilitate the study of liquids interacting with solid structures, such as walls or pores. Among other things, the program provides the option to generate a variety of different structures, including carbon walls and nanotubes and their boron nitride analogs, as well as the ability to analyze various structural properties of confined and interfacial liquids. In the case of the ionic liquid 1-butyl-3-methylimidazolium acetate in carbon nanotubes of different sizes, we demonstrate the abilities of our tool. The average density within the confinement highly depends on the carbon nanotube size, and it is generally lower than the density of the bulk liquid. The arrangement of the individual species within the tube also depends on size, with radial layers forming within the tubular confinement. The density is largely increased in the respective layers, while it is drastically reduced between the layers.

1. INTRODUCTION

Carbon materials have been extensively studied, with idealized structures such as pristine carbon walls and carbon nanotubes (CNTs)^{1–13} as well as complex porous structures.^{14–16} It has been observed that liquids in confinement and at interfaces behave significantly different than in bulk. For example, changes in the packing and the rearrangement dynamics within the liquid can be observed.^{3,11,16–20}

Ionic liquids (ILs), in combination with carbon materials, are of particular interest because they are attractive for the use in various electrochemical devices,^{21–25} especially high-performance electrical double-layer capacitors (EDLCs).^{17,26} ILs consist solely of ions and remain in the liquid state at room temperature. In these electrochemical systems, e.g., an IL in porous carbons, the confinement changes the physical and electrochemical properties, leading to a unique behavior. Furthermore, the capacitance of the electrode is dramatically enhanced when the pore size of the carbon material matches that of the ions.^{15,17,27} The underlying effects of this phenomena are not yet fully understood. Yet, it is known that the adjustment of ILs and nanoporous carbon materials has the potential to significantly improve the performance of EDLCs.^{28,29} Observing the molecular level ordering and analyzing the corresponding characteristics of a liquid inside sub-nanometer confinement is experimentally challenging, and support from theoretical studies are desirable. This in turn requires the availability of simple-to-use and comprehensive

software tools. Our novel software CONAN presented herein allows us to study liquids at the interface of solid structures, which are either walls or pores and which are modeled at an atomistic resolution. CONAN can generate a variety of different carbon and boron nitride structures and combine them with any liquid bulk system in order to create input simulation boxes for simulations. More importantly, it provides a set of analysis tools to evaluate trajectories with respect to the properties of liquids in confinement. Hereby, some functions and analysis options are already known from literature (e.g., the nanostructure build plugin in VMD³⁰), or they have been described in previous works.^{1,3,6,7,14,31–36} Further some novel functions of CONAN are also provided. Since it is desirable to have all the above-described functions available in one software tool, CONAN was developed as a publicly accessible software^{37,38} and is written in Python.³⁹ The program accesses some Python libraries and packages to optimize its performance. MDAnalysis^{40,41} is used to some extent to read trajectories and NumPy,⁴² PANDAS,⁴³ SciPy,⁴⁴ and NETWORKX⁴⁵ are used for faster calculation performances. The MATPLO-

Received: July 14, 2023

Published: October 31, 2023



LIB,⁴⁶ RDKit,⁴⁷ and PRETTYTABLE⁴⁸ packages are used to visualize the results, draw the identified molecules, and tabulate information regarding the investigated system and analysis results, respectively.

This article is structured into three main parts. First, the methodology needed for the production of solid structures, the setting up of a simulation box, and the respective analysis options are presented in [Section 2](#). Second and third, to illustrate exemplary features of our software, a case study of 1-butyl-3-methylimidazolium acetate ($[C_4C_1Im][OAc]$) within a set of differently sized carbon pores is presented with computational details given in [Section 3](#) and results shown in [Section 4](#).

2. METHODOLOGY

2.1. Structure Generator. The automatic generation of graphene, boron nitride, and related structures is an important step toward being able to study the systems without having to write a software tool each time or manually fixing the structures. Other than CONAN, there are other published plugins and programs that are able to produce a variety of different crystalline structures, such as structures of cellulose,⁵⁰ carbon walls, nanotubes, the corresponding boron nitride analogues³⁰ and more.^{51–53} Programs such as GOPY⁵⁴ and CoNTub^{55,56} allow for the functionalization of carbon walls and the merging of different CNTs. Still, the combination of a CNT and a graphene sheet has to be done manually so far to obtain structures as in [Figure 1g–j](#)—a feature that is now available in CONAN. Furthermore, it is also possible to dope all carbon structures with graphitic nitrogen, as well as to adjust units and bond lengths on the fly while generating the structures.

For all the carbon structures, the default value for the carbon–carbon distance is adjusted to $r_{C-C} = 142$ pm,⁵⁷ and for the boron nitride structures, the boron–nitrogen distance is set to $r_{B-N} = 144.6$ pm.⁵⁸ For the production of wall structures (e.g., [Figure 1a–d](#)), the desired dimensions are chosen by the user in x - and y -directions. Because it is important for subsequent simulations that periodic boundary conditions (PBC) are fulfilled in all the directions, the size is tuned accordingly. To this end, the program automatically produces structures that satisfy the PBC while being as close as possible to the given input. The box dimensions that need to be selected to fit the PBC are provided by CONAN. Additionally, it is possible to produce multiple, stacked layers. The stacking of the carbon sheets is carried out in a way that by shifting each consecutive layer, an ABA layering is obtained with the default interlayer distance of $r_{L-L} = 335$ pm.⁵⁷ In the case of the boron nitride analogue, successive layers are not shifted. Instead, the ABA layering is obtained by exchanging the positions of the boron and nitrogen atoms in consecutive layers, while the interlayer distance is set to $r_{L-L}^{BN} = 333$ pm.⁵⁸ CNTs and boron nitride nanotubes ([Figure 1e,f](#)) can be generated either in armchair or in zigzag conformation, while the length and the diameter of a tube is freely adjustable. The construction of a tube is done in such a way, that the PBCs are satisfied with respect to the direction of orientation. The given input length of the tube is thus adjusted slightly, similar to the one discussed for the carbon layers. The diameter of a (n,n) nanotube (armchair), or $(n,0)$ nanotube (zigzag) is defined via n , which is the number of atoms that build the circumference. Pore structures are constructed by merging walls and a nanotube of choice via two ways. One possibility is to produce

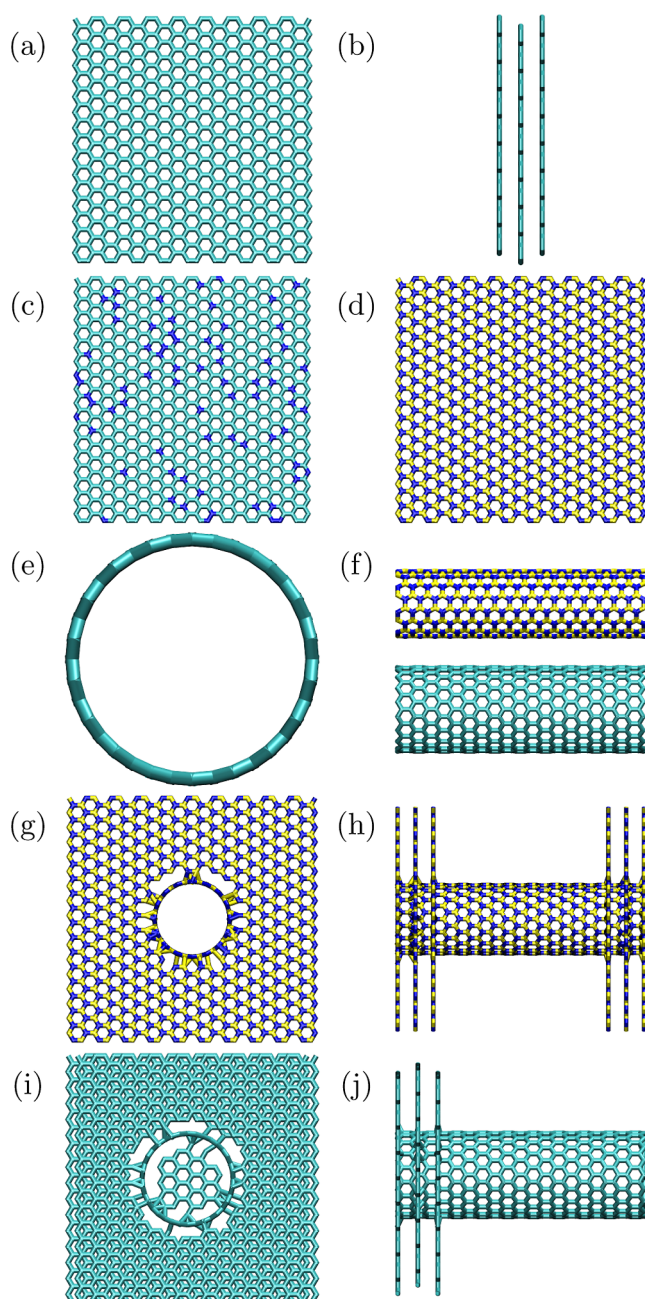


Figure 1. Variety of structures generated using CONAN. All the structures were visualized in bond representation using VMD.^{30,49} (a) Front view of a carbon wall. (b) Side view of multiple carbon layers, stacked in an ABA fashion. (c) Front view of a doped carbon wall with 10% graphitic nitrogen. (d) Front view of a boron nitride wall. (e) Front view of a (18,0) CNT. (f) Side view of a (8,8) boron nitride nanotube and a (18,0) CNT. (g) Front view of a boron nitride pore. (h) Side view of a boron nitride pore. (i) Front view of a closed carbon pore. (j) Side view of a closed carbon pore.

open-pore structures, where walls are attached to each open end of a given tube, while the atoms of the wall which cover openings are discarded ([Figure 1g,h](#)). The other option is to attach a wall on one side, while the other open end of the tube is closed ([Figure 1i,j](#)). The output file of a structure is given in xyz-format, either in units of Ångstrom, Bohr, or arbitrary units set by the user. All structures can be combined with any bulk liquids using CONAN to set up the desired system.

2.2. Snapshots of a Given Trajectory. Herein, all snapshots were visualized using the rendering plugin of VMD.^{30,49} With the aid of CONAN, one can cut out individual frames from a given trajectory file. It also allows to identify, characterize, and cut out a pore structure from a given frame adding the nanotubes center point. Extracting only the nanotube from the pore structure (Figure 2) is also

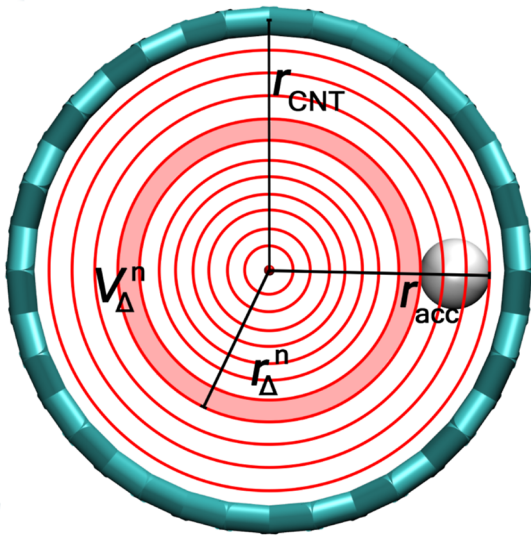


Figure 2. Front view of a (18,0) CNT with its center axis highlighted by the red dot in the center. Each increment describes the area between two red circles, which are the increment borders. The most displaced atom, in this case a hydrogen, is depicted with its van der Waals radius. r_{acc} describes the distance between the center point and the displaced atom, including its van der Waals radius. The figure was visualized using VMD,^{30,49} employing the bond model for the CNT (cyan) and the van der Waals radius model for the hydrogen atom (white).

possible. Additionally, one can extract the nanotube including the liquid that is confined within it, either atom- or molecule-wise. The molecule-wise extraction always considers complete molecules, even those that are only partially within the CNT. In the atom-wise extraction, only those atoms are considered that are within the confinement, without taking bonds into account.

2.3. Trajectory Analysis. There are established programs (such as TRAVIS^{59,60} or MDANALYSIS^{40,41}) that offer features for reading and analyzing trajectories. However, the available analysis options are typically designed for investigating bulk liquids and are often not applicable to anisotropic systems, such as liquids in confined environments. CONAN, on the other hand, is designed for the analysis of trajectories of anisotropic systems consisting of solid and liquid. A tool to identify all molecules and structures is implemented, allowing for an analysis to be performed individually for each molecular species. PBCs are thereby taken into account. In addition, the atoms in each unique molecule are labeled and images of the individual structures are generated. This makes it possible to perform each analysis exclusively for certain atoms of a molecule. The molecule recognition relies on one single frame of the trajectory; this automatically excludes the analysis of chemical reactions. Solid structures within the system are recognized by additionally analyzing a consecutive frame and labeling molecules as solids if they display no movement. The

solid structures therefore have to be kept frozen in position over the course of the simulation.

2.3.1. Radial Density Profiles. CONAN provides the option of computing radial density profiles. Thereby the space around the center axis of a tube is divided into n distinct radial increments as shown in Figure 2 by red circles, up to the wall of the nanotube ($r_{\Delta}^{\max} = r_{\text{CNT}}$). The volume of the n th increment (V_{Δ}^n) is computed by simplifying the tube to be a cylinder, using the length of the CNT (l_{CNT}) as its height and the following equations

$$V_{\text{cyl}}^n = \pi \cdot (r_{\Delta}^n)^2 \cdot l_{\text{CNT}} \quad (1)$$

$$V_{\Delta}^n = V_{\text{cyl}}^n - V_{\text{cyl}}^{n-1} = \pi \cdot l_{\text{CNT}} \cdot ((r_{\Delta}^n)^2 - (r_{\Delta}^{n-1})^2) \quad (2)$$

V_{cyl}^n is the volume of a cylinder of length l_{CNT} and the radius of the n th increment (r_{Δ}^n). V_{cyl}^{n-1} is the volume of the cylinder of the same length and the radius of the next smaller increment r_{Δ}^{n-1} . While scanning the whole trajectory, each atom inside the tube is identified, weighed by either its element mass or its partial charge, and the distance to the center axis (d_{rad}) is calculated. The identified atom is then assigned to the appropriate increment according to $r_{\Delta}^n < d_{\text{rad}} > r_{\Delta}^{n-1}$. After completing the scan, the average mass/charge density of the liquid ($\rho_{\Delta}^n / \rho(q)_{\Delta}^n$) in each increment is determined. This is achieved by dividing the total mass (m_{total}^n)/charge (q_{total}^n) obtained within a specific increment by the volume of that increment and the number of analyzed time steps (TS), using the following equations

$$\rho_{\Delta}^n = \frac{m_{\text{total}}^n}{V_{\Delta}^n \cdot \text{TS}} \quad (3)$$

$$\rho(q)_{\Delta}^n = \frac{q_{\text{total}}^n}{V_{\Delta}^n \cdot \text{TS}} \quad (4)$$

To refine the computed results, they can be normalized by dividing d_{rad} by the radius of the CNT (r_{CNT}). Additionally, mirroring the results is an option provided to illustrate the relationship between the obtained results and the image of a CNT. It is also possible to display the results in the form of a contour plot. An example is given in the Supporting Information, where the radial density of the IL within the confinement is shown for system 18.

2.3.2. Accessible Volume. The accessible volume inside a pore is characterized as the space that can be occupied by the atoms in the confinement. This is determined by scanning each frame of the trajectory to find the atom inside the confinement that is situated furthest with respect to its center axis, that is, closest to the wall of the tube. The accessible radius (r_{acc}) is then calculated by adding either one of the two options, the van der Waals radius⁶¹ or the covalent radius⁶² of the given element to the position of the atom. The accessible volume is computed using eq 1, where r_{Δ}^n is substituted by r_{acc} as the radius. The calculated accessible volume can be subsequently used to compute the axial density profile, which is discussed in the next section. If the analysis is performed only for a particular type of molecule, then the accessible radius will also be calculated only for that species in the system. When conducting this analysis, CONAN also provides the xyz-structure of the CNT, including the most displaced atom, as depicted in Figure 2.

2.3.3. Axial Density Profile. Another option is the calculation of an axial density profile along the entire

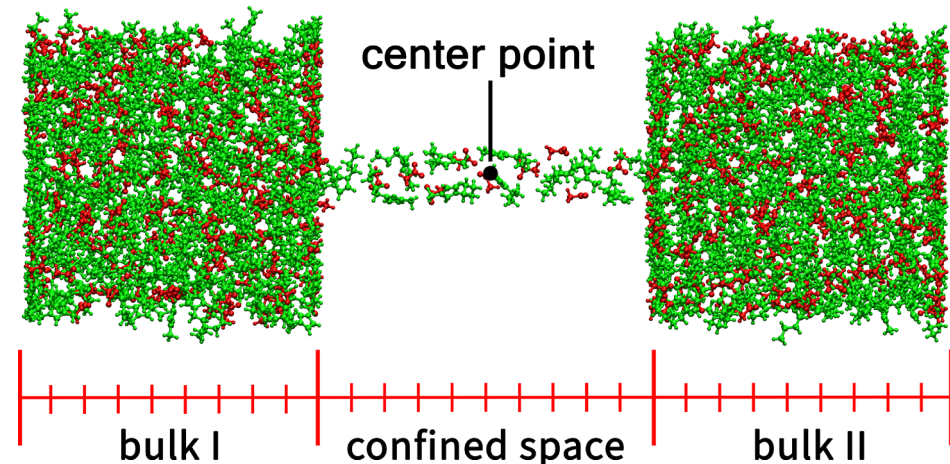


Figure 3. Side view of the simulation box with the incrementation areas depicted. The system was visualized using VMD,^{30,49} using a ball-and-stick model for the ions (anion: red, cation: green). The carbon walls and pores are not depicted.

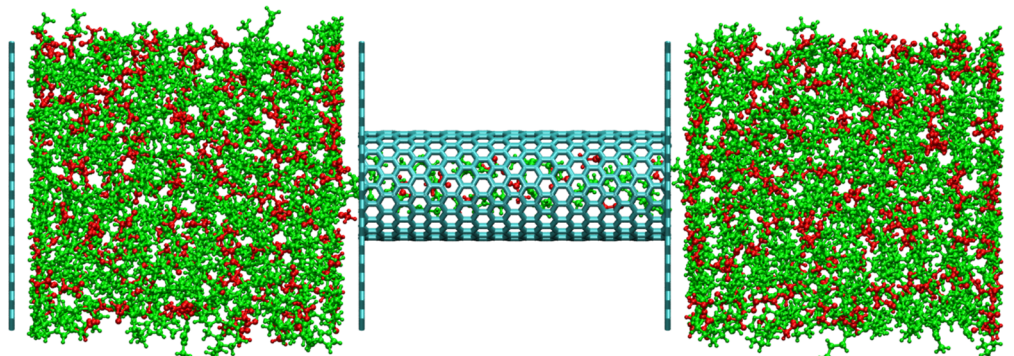


Figure 4. Exemplary system of two bulk phases with a (18,0) CNT in the center. The carbon walls on either sides act as pistons, applying 1 bar of pressure on the liquid. The IL is shown in a ball-and-stick model (anion: red, cation: green), while the carbon structures are shown with a bond model (blue). The system was visualized using VMD.^{30,49}

simulation box, including the bulk phases. To correctly compute the density inside the tube structure, the center axis must be oriented along the z axis in the simulation box. The volume of the CNT is calculated either using the accessible radius r_{acc} which is computed on the fly (Section 2.3.2) during the analysis, or using the CNTs' radius r_{CNT} . The radius of the CNT is defined as the distance between a carbon atom of the CNT and the center axis (Figure 2). The number of increments and therefore the respective volumes can be freely adjusted. As the volume of the respective increments in bulk and in confined space differ, multiple regions are defined in the simulation box (Figure 3). The number of increments subdivides the confined space and the bulk phases independently to ensure that an increment does not cover an area that is partially in the bulk and partially in the confined space. The entire trajectory is scanned and all atoms are sorted into a respective increment, weighed by its element mass. All obtained total increment masses are then divided by the number of frames used for the analysis and the respective increment volume to obtain the density profile.

The results can be further processed using CONAN. The binning within the pore can be increased by mirroring the obtained densities at the center point of the pore and calculate the average. In addition, the center of the pore can be set as origin on the axis.

3. COMPUTATIONAL DETAILS

3.1. Simulation Box. The simulation boxes (see Figure 4) were built employing CONAN, combining the previously produced carbon structures (see Section 2.1) with two reservoirs of the IL $[\text{C}_4\text{C}_1\text{Im}][\text{OAc}]$, each comprising 200 ion pairs. When the simulation box is built, a distance criterium assures that the individual pieces which are to be combined (e.g., pore and bulk) are merged with a space of 300 pm in between to avoid initial hotspots. The exact workflow is described in the Supporting Information.

3.2. Molecular Dynamics Simulations. Classical MD simulations of the pure IL $[\text{C}_4\text{C}_1\text{Im}][\text{OAc}]$ were carried out in order to study the behavior of the liquid in confined space of differently sized CNTs. A bulk simulation of the IL serves as a reference system. The IL was modeled using the atomistic CL&P force field,^{63,64} which has the same functional form as the OPLS-aa force field.⁶⁵ Electrostatic interactions are computed using the Ewald summation formalism, while the Lennard-Jones interaction potential was implemented to model interatomic interactions using Lorentz-Berthelot mixing rules up to the cutoff distance set to 12 Å. In case of the carbon structures, the potential parameters of Cole and Klein⁶⁶ were used. Unity charges of 1.0e were chosen for each ion. All simulations were carried out using the Metalwalls code⁶⁷ with the TS set to 1 fs. The bulk simulation was equilibrated for 2 ns in an NpT ensemble at 400 K, using a

cubic box containing 250 ion pairs of the IL before starting the subsequent production run of 10 ns in a canonical ensemble. The obtained density of the reference system $\rho_0 = 0.973 \text{ g/cm}^3$ is in close proximity to the experimental results, with a deviation below 2%.⁶⁸

For the simulations of the IL in confinement, two IL bulk boxes were merged with two carbon walls and different carbon pore structures as described in Section 3.1. Each system comprises a total of 400 ion pairs of the IL, two outer carbon walls, and the respective pore structure composed of a CNT with a carbon wall on each open end. As for the bulk system, a temperature of 400 K was adjusted. All carbon structures were kept rigid in the simulation. After the construction of the system (workflow in Supporting Information) and a preequilibration, the systems were further equilibrated for 1 ns in an $Np(z)T$ ensemble, where PBCs were applied in x - and y -directions, while the carbon walls on each side of the box posed as pistons, acting on the liquid with a force of 1 bar. After a final equilibration phase of 1 ns in a canonical ensemble, the production run of 10 ns was set, saving every 250th TS.

The carbon walls employed in the presented systems consist of 576 atoms and extend up to 3834 pm in x direction and 3935.2 pm in y direction with PBC applied in both. The employed pore structures composed of CNTs of different sizes are listed in Table 1. In case of the pores with a (16,0) CNT,

Table 1. For Each System, the Number of Atoms of the Implemented Pore, the Respective Employed CNT, Its Radius r_{CNT} , Its Length l_{CNT} and Its Volume V_{CNT} are Listed

system	no. atoms	CNT	r_{CNT} [pm]	l_{CNT} [pm]	V_{CNT} [10^6 pm^3]
12	1540	(12,0)	470	4130	2866
14	1600	(14,0)	548	4127	3894
16a	1654	(16,0)	626	4125	5078
16b	1782	(16,0)	626	4978	6128
16c	1974	(16,0)	626	6258	7704
18	1698	(18,0)	705	4123	6438
20	1750	(20,0)	783	4122	7939

three different systems were set up using CNTs of different length to check if the set lengths of approximately 4000 pm in z direction are sufficient to describe the confined space inside a CNT. Additionally, the input Metalwalls files are provided in the Supporting Information for total reproducibility.

4. CASE STUDY: IL INSIDE A PORE

4.1. Radial Density Profiles. **4.1.1. Mass Density.** Radial density profiles were calculated for each system to gain insight into the packing of the IL within differently sized nanopores, depicted in Figure 5. In case of the three systems with pores comprising a (16,0) CNT, only 16a is shown, because differences between the three CNTs of different length are negligible, see Supporting Information. Besides the overall density distributions for the IL (black), the individual contributions from the anion (red) and cation (blue) are depicted with the distances (d_{rad}) being normalized by the radius of the respective CNT (r_{CNT}). The obtained densities ρ are divided by the bulk density of the reference system ρ_0 and mirrored with respect to the CNT center. This is done to visualize the connection between the snapshots of the respective CNTs filled with IL and the obtained density profiles of Figure 5. Unsurprisingly, the larger contribution to

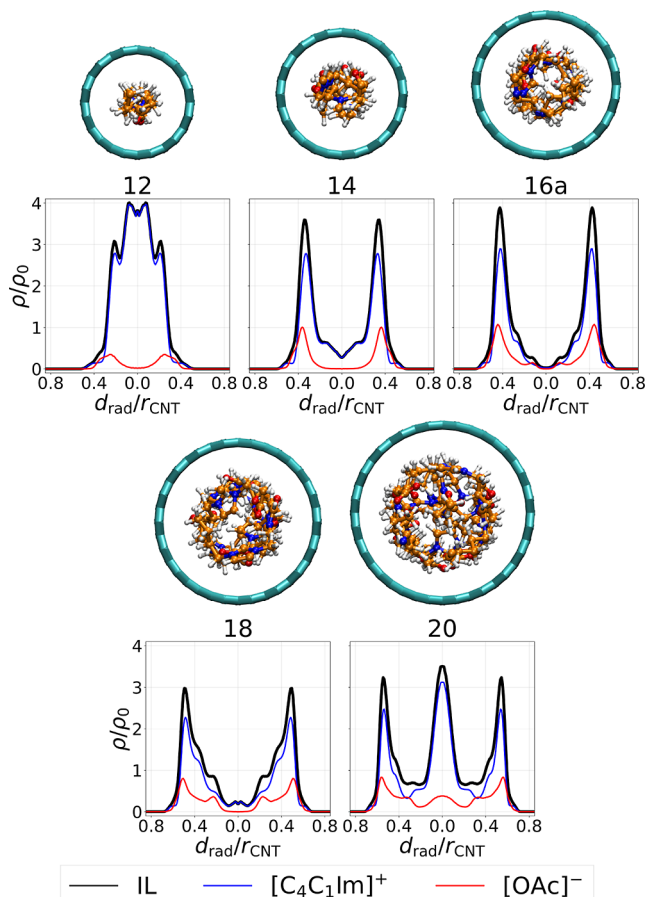


Figure 5. Radial mass density distributions of the IL inside the pores of systems 12, 14, 16a, 18, and 20. The overall density profile is shown in black, the individual contributions from the cation in blue, and from the anion in red. Above the respective plots: CNTs of the respective pores in a bond model (blue), the ions in a ball-and-stick representation (color code: carbon = orange, hydrogen = white, nitrogen = dark blue, oxygen = red). Please note, $1.0 d_{\text{rad}}/r_{\text{CNT}}$ marks the location of the CNT atoms.

the density profiles of the IL comes from the cation, because the molecular mass of the cation is larger compared to that of the acetate. Please note that over the course of the simulation, the number of the cations and anions inside the confinement may vary. Thus, especially for the smallest pore structures, the individual contributions change with respect to the filling of the pore. The shape of the individual ion density profiles is not affected.

In system 12, the $[\text{C}_4\text{C}_1\text{Im}]^+$ density profile shows that the cations are located at the CNTs center axis. The maxima at $|0.075| d_{\text{rad}}/r_{\text{CNT}}$ indicate just a minor shift toward the carbon wall. The nanotube and cation size therefore almost perfectly match, allowing only for minor adjustment in the cations radial position. The second set of maxima at $|0.215| d_{\text{rad}}/r_{\text{CNT}}$ also indicate that the rotational freedom of the cation with respect to the wall is hindered and a certain orientation toward the wall of the CNT is preferred. The density profile of the $[\text{OAc}]^-$ anion shows a more pronounced shift toward the carbon interface, with distinct maxima at $|0.255| d_{\text{rad}}/r_{\text{CNT}}$ while the density at the center is close to 0. Due to its smaller size, the anion has greater freedom to move within the confined space, enabling it to minimize the distance to the

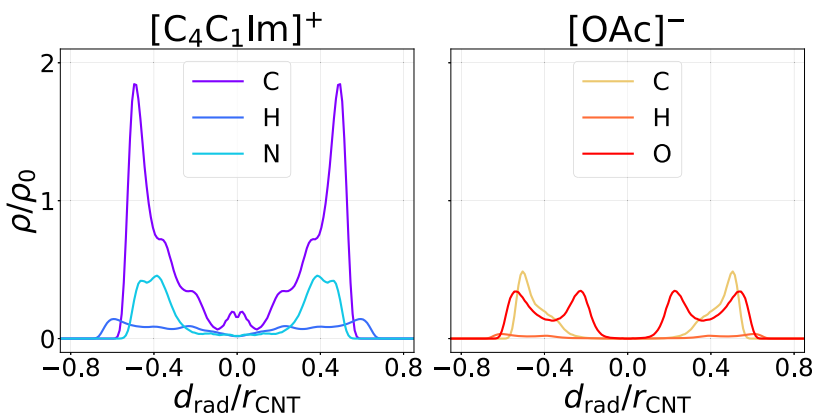


Figure 6. Radial mass density distributions of the elements in the individual ions inside the pore of system **18**. In the case of the cation, the distribution for carbon is shown in purple, for hydrogen in blue, and for nitrogen in cyan. For the anion, the distribution for carbon is shown in yellow, for hydrogen in orange, and for oxygen in red.

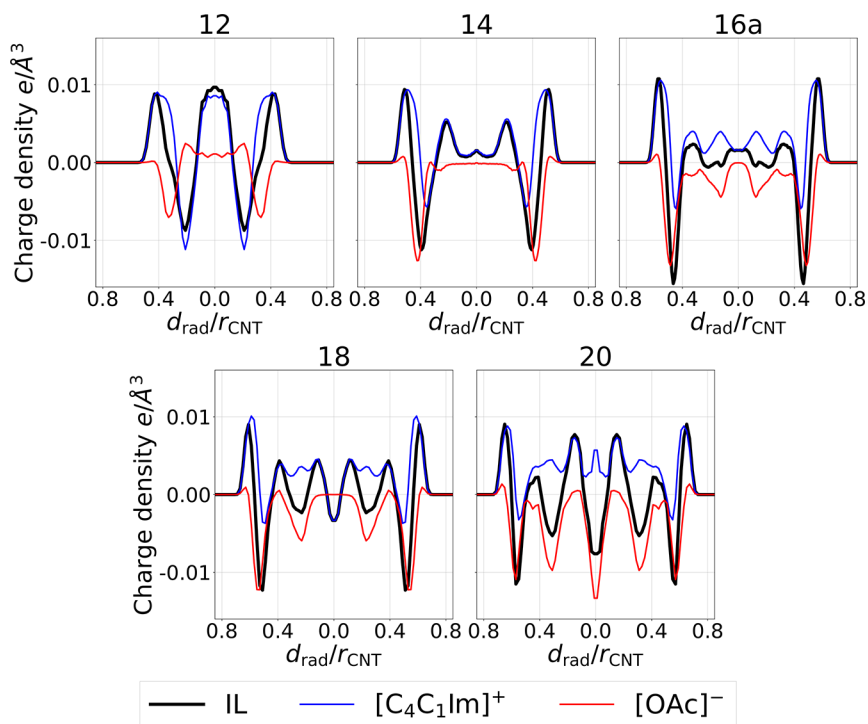


Figure 7. Radial charge density distributions of the IL inside the pores of systems **12**, **14**, **16a**, **18**, and **20**. The overall density profile is shown in black, the individual contributions from the cation in blue, and from the anion in red.

interface and thereby, maximize its interaction with the CNT wall.

The density in the center of the CNT is quadrupled compared to the bulk density, and quickly decays to values below 10% of the reference density for values $> 1.0455d_{\text{rad}}/r_{\text{CNT}}$, which corresponds to a distance of 214 pm from the center.

With increasing pore size, the packing of the IL within the pore changes to a tubular shape, which was also observed in other studies.^{69,70} A tubular shape means that the ions are shifted from the center to maximize the liquid–wall interactions, resulting in an increased density at the interface, while the density in the center is drastically decreased. The distances between the maxima in the density profiles correspond to the diameter of the tubular IL packing. In case of system **14**, this amounts to 378 pm (system **16a**: 532

pm; system **18**: 698 pm; system **20**: 853 pm). Interestingly, in the case of system **18**, the tubular arrangement of the IL gets an additional central contribution, that is, an increased density arises around the center axis compared to the smaller systems. This effect is especially present for the $[\text{OAc}]^-$ density profile, where four distinct maxima at $1.0225d_{\text{rad}}/r_{\text{CNT}}$ and $1.0505d_{\text{rad}}/r_{\text{CNT}}$ are present. This indicates the emergence of a second radial layer inside the confinement. These observations are supported by the largest investigated system, system **20**, where an additional maximum in the density profile is present at the center. It indicates the formation of a chain of IL species positioned in the center of the CNT, composing the second radial layer inside the confinement. The species in the center of the pore do not come into direct contact with the pore wall and presumably have different characteristics regarding diffusivity and conformation with regard to their counterparts directly at

the interface. Several previous works showed that species in the center of a given pore diffuse faster compared to species at the interface of the carbon structure.^{16,71,72} In the future, CONAN will also provide the possibility to study dynamic properties, such as diffusion, of the liquid to gain further insight into its behavior in confinement.

For a more precise determination regarding the positioning of the respective ions in the confinement, it is also possible to calculate the contributions of the individual atoms from each molecule. In the example of system 18, Figure 6 shows the individual contributions of the elements of the cation and the anion, respectively.

Based on the individual contributions, it can now be seen that, especially in the case of the cation, the largest $|d_{\text{rad}}/r_{\text{CNT}}|$ values in the density distribution of the respective ions can be attributed to the hydrogen atoms. In addition, the comparison between the distribution of the carbon atoms and that of the oxygen atoms from the anion is interesting. While the density profile of the oxygen splits and marks two preferred positions (0.25 and 0.55 $|d_{\text{rad}}/r_{\text{CNT}}|$) from the central axis, this is not the case for carbon with one maximum at 0.5 $|d_{\text{rad}}/r_{\text{CNT}}|$. It therefore becomes clear that there are not yet two different layers in system 18. The double peak of the oxygen distribution can therefore be explained by the fact that the anion is no longer oriented exclusively toward the pore wall, but that the carboxylate group also assumes a conformation perpendicular to the pore wall, in which an oxygen atom points toward the center axis.

4.1.2. Charge Density. The systems presented here have been modeled with standard force fields, therefore each atom of the ions has been assigned a fixed partial charge. The charges attributed to each atom are listed in Table S1 in the Supporting Information. In the case of the acetate anion, the oxygen atoms in particular are partially negatively charged, whereas the hydrogen atoms are partially positively charged. The carbon atom of the carboxylate group also carries a positive partial charge. In the cation, the positive charge is localized on the nitrogen and hydrogen atoms, while the carbon atoms bear partial negative charges. The charge density distribution functions therefore contain information about the accumulation of charges.

Radial charge density profiles were calculated for each system and are depicted in Figure 7. The charge density for the largest respective $|d_{\text{rad}}/r_{\text{CNT}}|$ values is positive for all systems, highlighting that the atoms closest to the pore walls are hydrogen atoms. Thereby, the curves of the IL and the cation are almost on top of each other, indicating the predominant contribution at these maximum distances stem from the cation. In the case of the anion, the charge density is also positive for the largest $|d_{\text{rad}}/r_{\text{CNT}}|$ values, which can be attributed to the hydrogen atoms of the methyl group. Nevertheless, the charge density drops to negative values for smaller $|d_{\text{rad}}/r_{\text{CNT}}|$ values, which can be assigned to the oxygen atoms of the carbonyl group and thus describes their positions within the pore. Therefore, the preferred position of the anion in the smallest systems, as already described in the radial density profile, is close to the pore wall and offset from the pore center. For increasing pore diameters, a second radial layer of the anion is formed within the confinement (system 16a and 18) and in system 20, even a third layer is observed, exactly in the center of the pore. It is also striking that the radial charge density distribution of each system behaves in an oscillating manner, with the outermost values always being positive as previously

stated. The number of oscillations thereby depends on the size of the pore, with the ordering becoming increasingly more complex for larger radii. The number of oscillations exceeds the number of anions and cations arranged side by side, which means that the orientation of the individual ions and their partial charges causes and amplifies these oscillating charge distributions. This assumption is further supported when looking at the charge densities of the individual ions. Here, too, the alternating course of the charge density can be clearly seen, which indicates a certain preferred positioning of the ions within the confined space.

4.2. Accessible Volume. The accessible radius and volume of each pore were computed for all systems and are listed in Table 2. For all investigated pores, the accessible

Table 2. The Obtained Accessible Radii r_{acc} , Calculated Employing the Respective Elements van der Waals Radii, and the Deviation Δr , Which is Defined as $1 - r_{\text{acc}}/r_{\text{CNT}}$ and Describes the Percentage the Accessible Radius is Smaller Compared to r_{CNT} ^a are listed

system	r_{acc} [pm]	Δr [%]	V_{acc} [10^6 pm^3]	ΔV [%]	ρ_{acc} [g/cm ³]	$\Delta \rho$ [%]
12	380	19.15	1874	34.6	0.394	59.5
14	462	15.54	2767	28.9	0.516	47.0
16a	539	13.90	3765	25.9	0.647	33.5
16b	540	13.85	4560	25.6	0.643	33.9
16c	547	12.65	5882	23.7	0.657	32.5
18	617	12.36	4931	23.3	0.644	33.8
20	702	10.43	6382	19.6	0.692	28.9

^aThe accessible volumes V_{acc} and the densities of the IL ρ_{acc} are also listed (see Figure 2). ΔV describes the percentage by which the volume is reduced, comparing V_{acc} to V_{CNT} ($1 - V_{\text{acc}}/V_{\text{CNT}}$). $\Delta \rho$ is defined by $1 - \rho_{\text{acc}}/\rho_0$ ($\rho_0 = 0.973 \text{ g/cm}^3$) and describes the percentage to which the density is decreased with respect to the reference bulk system.

radius r_{acc} is 80–90 pm smaller than the respective r_{CNT} . From visual observation of the most displaced atoms, it becomes apparent that the identified atoms are embedded in a hexagon of the carbons honeycomb structure, minimizing the ion–wall distance (see Figure S4 in the Supporting Information, showing the most displaced atom in system 14). For the pores in systems 16a–c, the obtained accessible radii differ slightly with r_{acc} being 8 pm larger in system 16c, where the pore is composed of the longest CNT, compared to system 16a with the shortest CNT. The deviation arises from the increased volume for the longer pore structures, leading to a higher amount of species in confinement and more sampling. Nonetheless, the difference is below 1.5%, therefore deviations are minor. $\Delta \rho$ is defined by $1 - \rho_{\text{acc}}/\rho_0$ and describes the percentage of the density that is reduced inside the respective confinement (Table 2). The results show a large decrease in density within all CNTs, with the effect becoming more drastic for smaller radii. In the (12,0) CNT, a reduction of the density of about 60% is achieved. This drops to about 30% for the larger CNTs studied, which is still significant. To evaluate the results, it should be mentioned that in the two smallest systems, anion and cation cannot exchange places, because the confinement restricts it. Thus, parts of the density decrease are due to the fact that ions of the same type can be adjacent inside the confinement, repelling each other and creating small gaps in between them. The arrangement of the ions within the CNTs is also described in detail in the next chapter. For the

systems **16a–c**, **18**, and **20**, the rearrangement of the ions within the confinement is possible, but nevertheless significant reductions in density are observed. In the comparison of the three systems, **16a–c**, it is also clear that despite better sampling for the longer pores, $\Delta\rho$ changes only slightly, with a maximum difference of 1.4%.

The occupancy of a given pore describes the proportion of the volume of the CNT (V_{CNT}) that can be accessed by the IL and is defined as $V_{\text{acc}}/V_{\text{CNT}}$. The results for the different systems, including systems **16b** and **16c** are plotted against the accessible radius r_{acc} of the respective CNT and are depicted in Figure 8. It is apparent that the occupancy increases steadily

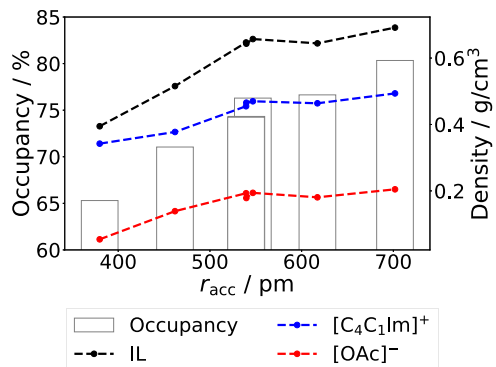


Figure 8. Occupancies ($V_{\text{acc}}/V_{\text{CNT}}$) and average densities of the IL inside the pore structures of different size, plotted against the accessible radius r_{acc} . The occupancies are shown as bars. The overall densities of the IL are depicted as a black graph, the contribution from the cation in blue, and from the anion in red.

for larger tube radii and highlights that the choice of the radius for the computation of the pore volume (r_{acc} or r_{CNT}) is crucial when calculating the density, especially for the smallest CNTs. Figure 8 also illustrates the computed average densities of the confined IL for CNTs of varying accessible radii. Smaller tube radii are accompanied by a significant reduction in average density, particularly for the two smallest pores. It is important to emphasize here again, that rearrangement of ions within these smallest pores is not possible, resulting in small cavities within the confined space. Therefore, the arrangement and filling of the pore are both critical points to consider when doing such an analysis.

4.3. Axial Density Profile. Besides the radial densities of the IL inside a pore structure, axial density profiles of the liquid were computed along the pore axis for all systems (Figure 9). A comparison between the systems **16a–c** is provided in the Supporting Information. In every system, between roughly 12100 and 16500 pm, the two bulk reservoirs of the IL show the typical density oscillations described in literature.^{1,7,32} In the center of the respective IL reservoirs (14300 pm), the oscillation of the density profile is hardly to no longer present, which shows that the imposed structuring of the IL at the interface has little influence on the structure in the respective reservoirs center. The density profile of system **12** shows that the center of the pore is filled with an anion surrounded by two cations. The mobility of the ions in the confinement appears to be small, since the density profile indicates defined areas in which the respective ion permanently resides. The open ends of the pore are occupied by additional cations that reside at a distance from the cations inside the pore. Gaps are present in between the adjacent cations, indicated by the minima in the

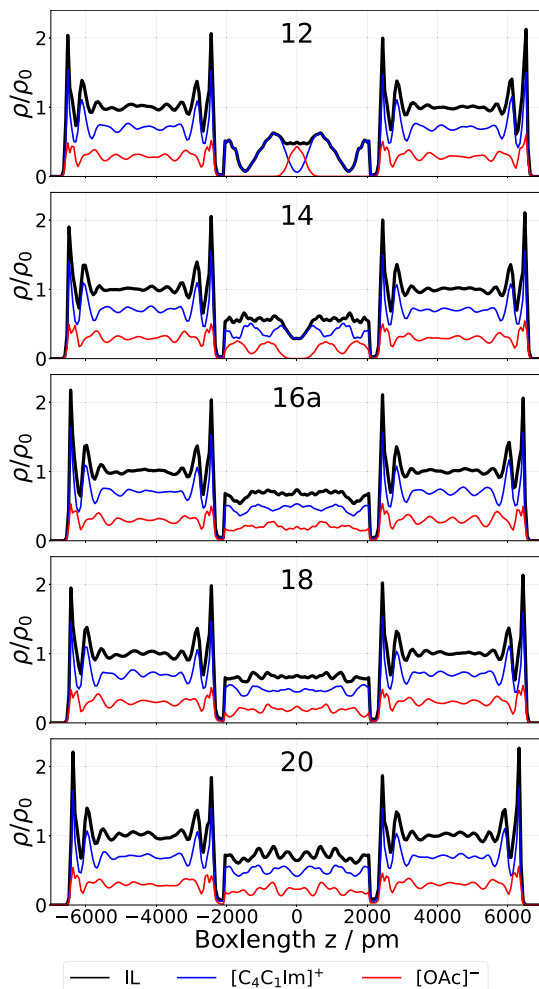


Figure 9. Axial density profiles of the liquid in systems **12**, **14**, **16a**, **18**, and **20** along the z -axis of the respective simulation boxes. The overall density of the IL is shown in black, the individual contributions from the cation in blue, and from the anion in red.

density plot at around 1500 pm. This shows that automatic filling of the smallest pores (systems **12** and **14**) during the simulation does not necessarily lead to an alternating packing of anions and cations within the confinement, because the rearrangement of the species is not possible. If the alternating arrangement is to be enforced, it is recommended to fill a pore from only one side, or do it manually.

For the IL confined in the (14,0) CNT, the alternating arrangement of the different species within the pore is also clearly visible from the respective density profiles, but with two cations being adjacent in the center of the pore. Comparable to system **12**, this also results in a gap within the pore between the ions of the same species, indicated by the reduced density of the individual ions at 0 pm, see Figure 9. Regarding the density profile of system **16a** and supported by the visual inspection of the corresponding trajectory, it is apparent that the rearrangement of ions within the confined space is possible for pores of these and larger sizes. The oscillation of the density profiles within the confinement is also significantly weakened. This applies to the overall density profile of the IL as well as to the contributions of the individual species, suggesting a different ordering and movement of the species within the confinement. The cross-section inside the CNT is thereby sufficiently large to allow for an anion and a cation to

reside next to each other. Very similar results were also obtained for system **18**. As shown in the analysis on radial densities, the IL has a very similar tubular packing within the pore. Again, the oscillating density profile is apparent in the (20,0) CNT regarding the IL and the individual contributions of the ions. This can be attributed to the presence of an additional central channel within the pore (as depicted in Figure 5), characterized by an alternating arrangement of anions and cations.

5. CONCLUSIONS

We presented a novel program for the purpose of investigating liquids in confinement. To showcase the options CONAN provides, a case study of 1-butyl-3-methylimidazolium acetate [C_4C_1Im][OAc] in well-defined pores of different size was conducted. Throughout this work, a workflow is described how to employ CONAN regarding the production of structures, the setup of solid–liquid systems of interest and the implemented analysis tools provided when studying liquids in confinement. Among other things, the program offers the possibility to calculate radial mass and charge densities of a fluid within nanotubes. In addition, the accessible volume of a tube can be determined, and an axial density can be calculated along a simulation box. Based on the generated data, further conclusions can be drawn, such as the calculation of the occupancy within a tube and the average density of a liquid in the confinement.

The case study of the IL shows that the liquid undergoes large changes in confinement compared to the bulk, with the change in density and packing being highly dependent on the pore size. When pore and ion size match, the ionic species align in a chain-like arrangement inside the pore, where the exchange of position between species is not possible. The structure of the IL changes to a tubular arrangement for larger pore sizes. The density of the IL is thereby increased at the IL–carbon interface, where the ionic species are shifted from the center to the carbon wall. This is accompanied by a decrease in density in the center of the pore, at least until the pore size is sufficiently large to allow for a second radial layer inside the confinement. It was also shown, that the overall density of the IL inside the confined structures is decreased, with the effect diminishing for increasing pore sizes.

In the future, the program will be extended to provide additional options to study MD trajectories. It is planned to extend the program with respect to the analysis of the coordination environment of a confined liquid and the calculation of diffusion properties. It is also planned to extend the structure building tool to other structures and materials.

■ ASSOCIATED CONTENT

Data Availability Statement

The code of METALWALLS is open source and freely available. The same is valid for CONAN, with the program being provided on our GitHub channel including example trajectories.

SI Supporting Information

The Supporting Information is available free of charge at <https://pubs.acs.org/doi/10.1021/acs.jcim.3c01075>.

Example radial density contour plot of system **18**, partial charges of the applied force field, exemplary figures of the most displaced atom from the accessible volume analysis of system **14**, radial charge and mass density

profiles of systems **16a–c**, and axial mass density profiles of systems **16a–c** ([PDF](#))

■ AUTHOR INFORMATION

Corresponding Author

Barbara Kirchner – Mulliken Center for Theoretical Chemistry, Rheinische Friedrich-Wilhelms-Universität Bonn, D-53115 Bonn, Germany; orcid.org/0000-0001-8843-7132; Email: kirchner@thch.uni-bonn.de

Author

Leonard Dick – Mulliken Center for Theoretical Chemistry, Rheinische Friedrich-Wilhelms-Universität Bonn, D-53115 Bonn, Germany; orcid.org/0000-0002-5596-9498

Complete contact information is available at:

<https://pubs.acs.org/10.1021/acs.jcim.3c01075>

Notes

The authors declare no competing financial interest.

■ ACKNOWLEDGMENTS

The authors thank the Max Planck institute of colloids and interfaces within the project “ERC Sys MoMA-STOR” (grant agreement no. 951513) for financial support. They gratefully acknowledge the access to the Bonna cluster hosted by the University of Bonn.

■ REFERENCES

- (1) Wang, G. J.; Hadjiconstantinou, N. G. Molecular mechanics and structure of the fluid-solid interface in simple fluids. *Phys. Rev. Fluids* **2017**, *2*, 094201.
- (2) Ingebrigtsen, T. S.; Dyre, J. C. The impact range for smooth wall–liquid interactions in nanoconfined liquids. *Soft Matter* **2014**, *10*, 4324–4331.
- (3) Aydin, F.; Moradzadeh, A.; Bilodeau, C. L.; Lau, E. Y.; Schwegler, E.; Aluru, N. R.; Pham, T. A. Ion Solvation and Transport in Narrow Carbon Nanotubes: Effects of Polarizability, Cation π Interaction, and Confinement. *J. Chem. Theory Comput.* **2021**, *17*, 1596–1605.
- (4) Losey, J.; Kannam, S. K.; Todd, B. D.; Sadus, R. J. Flow of water through carbon nanotubes predicted by different atomistic water models. *J. Chem. Phys.* **2019**, *150*, 194501.
- (5) da Silva, L. B. Structural and dynamical properties of water confined in carbon nanotubes. *J. Nanostruct. Chem.* **2014**, *4*, 104.
- (6) Frank, M.; Drikakis, D.; Asproulis, N. Thermal conductivity of nanofluid in nanochannels. *Microfluid. Nanofluidics* **2015**, *19*, 1011–1017.
- (7) Carter, B. M.; Royall, C. P.; Dyre, J. C.; Ingebrigtsen, T. S. Isomorphs in nanoconfined liquids. *Soft Matter* **2021**, *17*, 8662–8677.
- (8) Rikhtehgaran, S.; Lohrasebi, A. Water desalination by a designed nanofilter of graphene-charged carbon nanotube: A molecular dynamics study. *Desalination* **2015**, *365*, 176–181.
- (9) Clark, J. K.; Paddison, S. J. Ab initio molecular dynamics simulations of water and an excess proton in water confined in carbon nanotubes. *Phys. Chem. Chem. Phys.* **2014**, *16*, 17756–17769.
- (10) Ruggeri, M.; Reeves, K.; Hsu, T.-Y.; Jeanmairet, G.; Salanne, M.; Pierleoni, C. Multi-scale simulation of the adsorption of lithium ion on graphite surface: From quantum Monte Carlo to molecular density functional theory. *J. Chem. Phys.* **2022**, *156*, 094709.
- (11) Chatzichristos, A.; Hassan, J. Current Understanding of Water Properties inside Carbon Nanotubes. *Nanomaterials* **2022**, *12*, 174.
- (12) Merlet, C.; Salanne, M.; Rotenberg, B.; Madden, P. A. Imidazolium ionic liquid interfaces with vapor and graphite: Interfacial tension and capacitance from coarse-grained molecular simulations. *J. Phys. Chem. C* **2011**, *115*, 16613–16618.

- (13) Bordes, E.; Szala-Bilnik, J.; Pádua, A. A. H. Exfoliation of graphene and fluorographene in molecular and ionic liquids. *Faraday Discuss.* **2018**, *206*, 61–75.
- (14) Simoncelli, M.; Ganfoud, N.; Sene, A.; Haefele, M.; Daffos, B.; Taberna, P. L.; Salanne, M.; Simon, P.; Rotenberg, B. Blue Energy and Desalination with Nanoporous Carbon Electrodes: Capacitance from Molecular Simulations to Continuous Models. *Phys. Rev. X* **2018**, *8*, 021024.
- (15) Merlet, C.; Rotenberg, B.; Madden, P. A.; Taberna, P. L.; Simon, P.; Gogotsi, Y.; Salanne, M. On the molecular origin of supercapacitance in nanoporous carbon electrodes. *Nat. Mater.* **2012**, *11*, 306–310.
- (16) Lahrar, E. H.; Belhboub, A.; Simon, P.; Merlet, C. Ionic Liquids under Confinement: From Systematic Variations of the Ion and Pore Sizes toward an Understanding of the Structure and Dynamics in Complex Porous Carbons. *ACS Appl. Mater. Interfaces* **2020**, *12*, 1789–1798.
- (17) Yan, R.; Antonietti, M.; Oschatz, M. Toward the Experimental Understanding of the Energy Storage Mechanism and Ion Dynamics in Ionic Liquid Based Supercapacitors. *Adv. Energy Mater.* **2018**, *8*, 1800026–1800112.
- (18) Elbourne, A.; Voitchovsky, K.; Warr, G. G.; Atkin, R. Ion structure controls ionic liquid near-surface and interfacial nanostructure. *Chem. Sci.* **2015**, *6*, 527–536.
- (19) Hayes, R.; Warr, G. G.; Atkin, R. Structure and Nanostructure in Ionic Liquids. *Chem. Rev.* **2015**, *115*, 6357–6426.
- (20) Li, Z.; Misra, R. P.; Li, Y.; Yao, Y.-C.; Zhao, S.; Zhang, Y.; Chen, Y.; Blankschtein, D.; Noy, A. Breakdown of the Nernst-Einstein relation in carbon nanotube porins. *Nat. Nanotechnol.* **2023**, *18*, 177–183.
- (21) Liu, Y. M.; Tian, W.; Jia, Y. X.; Yue, H. Y. The use of CE ECL with ionic liquid for the determination of drug alkaloids and applications in human urine. *Electrophoresis* **2009**, *30*, 1406–1411.
- (22) MacFarlane, D. R.; Tachikawa, N.; Forsyth, M.; Pringle, J. M.; Howlett, P. C.; Elliott, G. D.; Davis, J. H.; Watanabe, M.; Simon, P.; Angell, C. A. Energy applications of ionic liquids. *Energy Environ. Sci.* **2014**, *7*, 232–250.
- (23) Dick, L.; Stettner, T.; Liu, Y.; Liu, S.; Kirchner, B.; Balducci, A. Hygroscopic protic ionic liquids as electrolytes for electric double layer capacitors. *Energy Storage Mater.* **2022**, *53*, 744–753.
- (24) Lin, Z.; Goikolea, E.; Balducci, A.; Naoi, K.; Taberna, P. L.; Salanne, M.; Yushin, G.; Simon, P. Materials for supercapacitors: When Li-ion battery power is not enough. *Mater. Today* **2018**, *21*, 419–436.
- (25) Ludwig, R.; Maginn, E.; Balasubramanian, S. Editorial: Ionic Liquids: The Fundamentals and Forces Driving Their Rise. *ChemPhysChem* **2012**, *13*, 1603.
- (26) Antonietti, M.; Chen, X.; Yan, R.; Oschatz, M. Storing electricity as chemical energy: beyond traditional electrochemistry and double-layer compression. *Energy Environ. Sci.* **2018**, *11*, 3069–3074.
- (27) Kondrat, S.; Georgi, N.; Fedorov, M. V.; Kornyshev, A. A. A superionic state in nano-porous double-layer capacitors: Insights from Monte Carlo simulations. *Phys. Chem. Chem. Phys.* **2011**, *13*, 11359–11366.
- (28) Feng, G.; Qiao, R.; Huang, J.; Dai, S.; Sumpter, B. G.; Meunier, V. The importance of ion size and electrode curvature on electrical double layers in ionic liquids. *Phys. Chem. Chem. Phys.* **2011**, *13*, 1152–1161.
- (29) Huang, J.; Sumpter, B. G.; Meunier, V. Theoretical model for nanoporous carbon supercapacitors. *Angew. Chem., Int. Ed.* **2008**, *47*, 520–524.
- (30) Humphrey, W.; Dalke, A.; Schulten, K. VMD – Visual Molecular Dynamics. *J. Mol. Graph.* **1996**, *14*, 33–38.
- (31) Salanne, M. Ionic Liquids for Supercapacitor Applications. *Top. Curr. Chem.* **2017**, *375*, 63.
- (32) Ingebrigtsen, T. S.; Dyre, J. C. The impact range for smooth wall–liquid interactions in nanoconfined liquids. *Soft Matter* **2014**, *10*, 4324–4331.
- (33) Park, S.; McDaniel, J. G. Interference of electrical double layers: Confinement effects on structure, dynamics, and screening of ionic liquids. *J. Chem. Phys.* **2020**, *152*, 074709.
- (34) Scalfi, L.; Salanne, M.; Rotenberg, B. Molecular Simulation of Electrode-Solution Interfaces. *Annu. Rev. Phys. Chem.* **2021**, *72*, 189–212.
- (35) Chatzichristos, A.; Hassan, J. Current Understanding of Water Properties inside Carbon Nanotubes. *Nanomaterials* **2022**, *12*, 174.
- (36) Fu, Q.; Nabok, D.; Draxl, C. Energy-Level Alignment at the Interface of Graphene Fluoride and Boron Nitride Monolayers: An Investigation by Many-Body Perturbation Theory. *J. Phys. Chem. C* **2016**, *120*, 11671–11678.
- (37) CONAN—GitHub repository. <https://github.com/kirchners-manta/conan>, (accessed Aug 22, 2023).
- (38) CONAN—Manual. <https://con-an.readthedocs.io/en/latest>, (accessed Aug 22, 2023).
- (39) Van Rossum, G.; Drake, F. L. *Python 3 Reference Manual*; CreateSpace: Scotts Valley, CA, 2009.
- (40) Michaud-Agrawal, N.; Denning, E. J.; Woolf, T. B.; Beckstein, O. MDAnalysis: A toolkit for the analysis of molecular dynamics simulations. *J. Comput. Chem.* **2011**, *32*, 2319–2327.
- (41) Gowers, R. J.; Linke, M.; Barnoud, J.; Reddy, T. J. E.; Melo, M. N.; Seyler, S. L.; Domański, J.; Dotson, D. L.; Buchoux, S.; Kenney, I. M.; Beckstein, O. MDAnalysis: A Python Package for the Rapid Analysis of Molecular Dynamics Simulations. *Proceedings of the 15th Python in Science Conference*; SciPy, 2016; Vol. 98, p 105.
- (42) Harris, C. R.; Millman, K. J.; van der Walt, S. J.; Gommers, R.; Virtanen, P.; Cournapeau, D.; Wieser, E.; Taylor, J.; Berg, S.; Smith, N. J.; Kern, R.; Picus, M.; Hoyer, S.; van Kerkwijk, M. H.; Brett, M.; Haldane, A.; del Rio, J. F.; Wiebe, M.; Peterson, P.; Gérard-Marchant, P.; Sheppard, K.; Reddy, T.; Weckesser, W.; Abbasi, H.; Gohlke, C.; Oliphant, T. E. Array programming with NumPy. *Nature* **2020**, *585*, 357–362.
- (43) McKinney, W. Data Structures for Statistical Computing in Python. *Proceedings of the 9th Python in Science Conference*; SciPy, 2010; Vol. 445, pp 51–56.
- (44) Virtanen, P.; Gommers, R.; Oliphant, T. E.; Haberland, M.; Reddy, T.; Cournapeau, D.; Burovski, E.; Peterson, P.; Weckesser, W.; Bright, J.; van der Walt, S. J.; Brett, M.; Wilson, J.; Millman, K. J.; Mayorov, N.; Nelson, A. R. J.; Jones, E.; Kern, R.; Larson, E.; Carey, C. J.; Polat, İ.; Feng, Y.; Moore, E. W.; VanderPlas, J.; Laxalde, D.; Perktold, J.; Cimrman, R.; Henriksen, I.; Quintero, E. A.; Harris, C. R.; Archibald, A. M.; Ribeiro, A. H.; Pedregosa, F.; van Mulbregt, P.; et al. SciPy 1.0: fundamental algorithms for scientific computing in Python. *Nat. Methods* **2020**, *17*, 261–272.
- (45) Hagberg, A. A.; Schwart, D. A.; Swart, P. J. *Exploring Network Structure, Dynamics, and Function Using NetworkX*; Los Alamos National Lab: Los Alamos, NM (United States), 2008.
- (46) Hunter, J. D. Matplotlib: A 2D Graphics Environment. *Comput. Sci. Eng.* **2007**, *9*, 90–95.
- (47) Landrum, G. RDKit: Open-Source Cheminformatics Software, 2010. <https://www.rdkit.org/> (accessed 22 Aug 2023).
- (48) PrettyTable. <https://pypi.org/project/prettytable>, (accessed Aug 22, 2023).
- (49) Stone, J. E. An efficient library for parallel ray tracing and animation. M.Sc. Thesis; University of Missouri, 1998; p 1747.
- (50) Gomes, T. C. F.; Skaf, M. S. Cellulose-Builder: A toolkit for building crystalline structures of cellulose. *J. Comput. Chem.* **2012**, *33*, 1338–1346.
- (51) Diudea, M. V.; Nagy, C. L.; Silaghi-Dumitrescu, I.; Graovac, A.; Janežič, D.; Vikić-Topić, D. Periodic cages. *J. Chem. Inf. Model.* **2005**, *45*, 293–299.
- (52) Hanwell, M.; Curtis, D.; Lonie, D.; Vandermeersch, T.; Zurek, E.; Hutchison, G. Avogadro: an advanced semantic chemical editor, visualization, and analysis platform. *J. Cheminf.* **2012**, *4*, 17.
- (53) Momma, K.; Izumi, F. VESTA: a three-dimensional visualization system for electronic and structural analysis. *J. Appl. Crystallogr.* **2008**, *41*, 653–658.

- (54) Muraru, S.; Burns, J. S.; Ionita, M. GOPY: A tool for building 2D graphene-based computational models. *SoftwareX* **2020**, *12*, 100586.
- (55) Melchor, S.; Dobado, J. A. CoNTub: An algorithm for connecting two arbitrary carbon nanotubes. *J. Chem. Inf. Comput. Sci.* **2004**, *44*, 1639–1646.
- (56) Melchor, S.; Martin-Martinez, F. J.; Dobado, J. A. CoNTub v2.0 - Algorithms for constructing C 3-symmetric models of three-nanotube junctions. *J. Chem. Inf. Model.* **2011**, *51*, 1492–1505.
- (57) Trucano, P.; Chen, R. Structure of graphite by neutron diffraction. *Nature* **1975**, *258*, 136–137.
- (58) Majety, S.; Cao, X. K.; Dahal, R.; Pantha, B. N.; Li, J.; Lin, J. Y.; Jiang, H. X. Semiconducting hexagonal boron nitride for deep ultraviolet photonics. *Quantum Sensing and Nanophotonic Devices IX*; SPIE, 2012; Vol. 8268, p 82682R.
- (59) Brehm, M.; Kirchner, B. TRAVIS - A Free Analyzer and Visualizer for Monte Carlo and Molecular Dynamics Trajectories. *J. Chem. Inf. Model.* **2011**, *51*, 2007–2023.
- (60) Brehm, M.; Thomas, M.; Gehrke, S.; Kirchner, B. TRAVIS—A free analyzer for trajectories from molecular simulation. *J. Chem. Phys.* **2020**, *152*, 164105.
- (61) Bondi, A. van der Waals Volumes and Radii. *J. Phys. Chem.* **1964**, *68*, 441–451.
- (62) Cordero, B.; Gómez, V.; Platero-Prats, A. E.; Revés, M.; Echeverría, J.; Cremades, E.; Barragán, F.; Alvarez, S. Covalent radii revisited. *Dalton Trans.* **2008**, 2832–2838.
- (63) Lopes, J. N. C.; Deschamps, J.; Pádua, A. A. H. Modeling Ionic Liquids Using a Systematic All-Atom Force Field. *J. Phys. Chem. B* **2004**, *108*, 11250–12047.
- (64) Lopes, J. N. C.; Pádua, A. Molecular Force Field for Ionic Liquids Composed of Triflate or Bistriflylimide Anions. *J. Phys. Chem. B* **2004**, *108*, 16893–16898.
- (65) Jorgensen, W. L.; Tirado-Rives, J. The OPLS [optimized potentials for liquid simulations] potential functions for proteins, energy minimizations for crystals of cyclic peptides and crambin. *J. Am. Chem. Soc.* **1988**, *110*, 1657–1666.
- (66) Cole, M. W.; Klein, J. R. The interaction between noble gases and the basal plane surface of graphite. *Surf. Sci.* **1983**, *124*, 547–554.
- (67) Marin-Lafèche, A.; Haefele, M.; Scalfi, L.; Coretti, A.; Dufils, T.; Jeanmairet, G.; Reed, S.; Serva, A.; Berthin, R.; Bacon, C.; Bonella, S.; Rotenberg, B.; Madden, P.; Salanne, M. MetalWalls: A classical molecular dynamics software dedicated to the simulation of electrochemical systems. *J. Open Source Softw.* **2020**, *5*, 2373.
- (68) Safarov, J.; Geppert-Rybczyńska, M.; Kul, I.; Hassel, E. Thermophysical properties of 1-butyl-3-methylimidazolium acetate over a wide range of temperatures and pressures. *Fluid Phase Equil.* **2014**, *383*, 144–155.
- (69) Zeng, Y.; Li, K.; Zhu, Q.; Wang, J.; Cao, Y.; Lu, S. Capture of CO₂ in carbon nanotube bundles supported with room-temperature ionic liquids: A molecular simulation study. *Chem. Eng. Sci.* **2018**, *192*, 94–102.
- (70) Guan, Y.; Chen, W.; Zhang, J.; Yang, F.; Du, C.; Zhang, X.; Deng, Y. Ionic Liquid Filled Single-Walled Carbon Nanotubes for Flow-Induced Energy Harvesting. *J. Phys. Chem. C* **2019**, *123*, 6981–6988.
- (71) Rajput, N. N.; Monk, J.; Singh, R.; Hung, F. R. On the influence of pore size and pore loading on structural and dynamical heterogeneities of an ionic liquid confined in a slit nanopore. *J. Phys. Chem. C* **2012**, *116*, 5169–5181.
- (72) Chio, C. C.; Tse, Y. L. S. Hindered Diffusion near Fluid-Solid Interfaces: Comparison of Molecular Dynamics to Continuum Hydrodynamics. *Langmuir* **2020**, *36*, 9412–9423.